Strojniški vestnik - Journal of Mechanical Engineering 54(2008)10, 693-706
UDC 62-233.1
Paper received: 14.06.2007
Paper accepted: 07.07.2008

Numerical and Experimental Analysis of a Shaft Bow Influence on a Rotor to Stator Contact Dynamics

Sanjin Braut [1,*] - Roberto Žigulić[1] - Mirko Butković[2]
[1] University of Rijeka, Faculty of Engineering, Rijeka, Croatia
[2] Polytechnic of Karlovac, Karlovac, Croatia

The shaft bow problem presents a real situation especially in case of slender rotors. This paper investigates the shaft bow influence on the rotor-stator contact dynamics. For this purpose the rotor is described as a simple Jeffcott model and the stator as an elastically suspended rigid ring. To test the numerical model, except a usual run down analysis, an emergency shut down after the sudden rotor unbalance increase is also analyzed. Numerical integration is carried out by the fourth-order Runge-Kutta method. Two different normal force models for the rotor-stator interaction are analyzed. For analyzed parameters, both linear and nonlinear (Hunt and Crossley), normal force models gave similar rotor and stator responses. To confirm some of the results and to tune the numerical model, the experimental investigation on the test rig was conducted.

Keywords: rotor-stator contact, shaft bow, numerical simulations, rotor vibration, vibration measurements

0 INTRODUCTION

Contact or rub between rotor and stator is one of the most intensive research subjects in rotor dynamics. Most papers which are considering the rotor-stator contact phenomena can be classified in rigid rotor disc-rigid stator contact [1] to [3], bladed disc-stator contacts [4] and rotor-stator contact in retainer bearings when the rotor is supported by active magnetic bearings [5] and [6]. Choy and Padovan [1] developed a general analytical rub model using the following assumptions: simple Jeffcott rotor model, linear stiffness and damping characteristics, rigid casing supported by springs acting in the radial direction, mass inertia of the casing small enough to be neglected, simple Coulomb friction and onset of rub caused by unbalance. Bartha [2] performed an extensive numerical and experimental research of the backward whirl of rotors considering the rigid and elastically suspended stator. Von Grol and Ewins compared measurements and simulations for a windmilling imbalance in aero-engines which is very similar to the classical rotor to stator contact. They have revealed the rotor response rich in different subharmonics. Influence of torsion on the rotor-stator contact was introduced by Edwards et al. [7]. Attention was paid to the effects of torsion on a steady state response of a system experiencing rotor to stator contact. The analyzed Jeffcott rotor model had only 3 degrees of freedom – d.o.f. because the stator was assumed to be rigid. Žigulić et al. [8] considered nonlinear dynamics of a rotor supported by two dry-friction bearings. The rotor was modeled with FEM-Finite element method and the obtained nonlinear system was integrated with Hilbert-Hughes-Taylor – HHT α method.

Karpenko et al. [9] have shown how the preloading of the snubber ring could stabilize the dynamic response of the rotor. Theoretical predictions of the two-degrees-of-freedom Jeffcott rotor model with the preloaded snubber ring subjected to out-of-balance excitation was studied in [10], while an experimental verification with special attention to the analysis of the shaft rotational speed (excitation frequency) as well as different eccentricities and preloading was given in [11].

This paper considers the contact between the rotor, with a bowed shaft, and the stator at the position of rotor disc (seal), after the appearance of sudden unbalance due to blade loss. Linear and nonlinear models of the normal contact force are compared for different shaft bow – mass unbalance combinations. In this study, not only lateral but also torsional d.o.f. are taken into account allowing the additional extension of the

*Corr. Author's Address: University of Rijeka, Faculty of Engineering, Vukovarska 58, HR-51000, Rijeka, Croatia, sanjin.braut@riteh.hr

model with mechanical model of the induction motor. Results of numerical simulations and experiments are presented and compared using the rotor and stator responses in time domain, spectral maps and rotor orbits

1 MODELING OF THE ROTOR-STATOR SYSTEM

A rather simple mechanical model for the rotor-stator interaction description is used. The rotor is described by Jeffcott model with a shaft bow while the stator is modeled as an elastically suspended rigid ring. Except traditional consideration of the rotor lateral d.o.f. (x_r, y_r), torsional d.o.f. (φ_r) is taken into account allowing an extension of the model with torsional d.o.f. of the induction motor (φ_m) as well as appropriate mechanical model. To keep consistency of the described consideration the stator had additional three d.o.f., two lateral (x_s, y_s) and one torsional (φ_s). Fig. 1 shows the considered rotor-stator system. Next sections briefly discuss the differential equations of motion, the contact model and mechanical model of the induction motor.

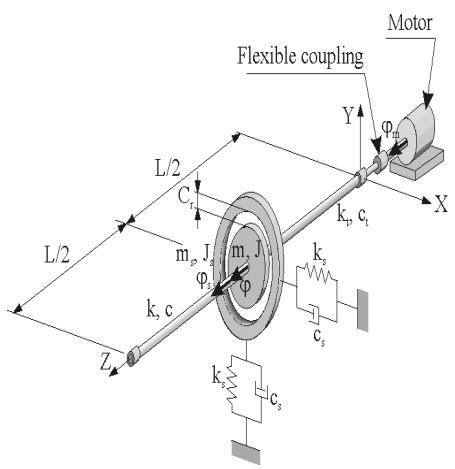

Fig.1. *Extended Jeffcott rotor model*

1.1. Differential equations of motion

The equations of motion for the system described above can be derived using the Lagrange equations and have the following form:

$$
\begin{aligned}
&m_r\ddot{x}_r + c_r\dot{x}_r + k_r x_r = m_r e\dot{\varphi}^2\cos\varphi + m_r e\ddot{\varphi}\sin\varphi + k_r x_{r0} - F_{Cx}\\
&m_r\ddot{y}_r + c_r\dot{y}_r + k_r y_r = m_r e\dot{\varphi}^2\sin\varphi - m_r e\ddot{\varphi}\cos\varphi + k_r y_{r0} - F_{Cy}\\
&J_r\ddot{\varphi}_r + c_{rt}\left(\dot{\varphi}_r - \dot{\varphi}_m\right) + k_{rt}\left(\varphi_r - \varphi_m\right) = M_{fr1} - M_C\\
&m_s\ddot{x}_s + c_s\dot{x}_s + k_s x_s = F_{Cx}\\
&m_s\ddot{y}_s + c_s\dot{y}_s + k_s y_s = F_{Cy}\\
&J_s\ddot{\varphi}_s + c_{st}\dot{\varphi}_s + k_{st}\varphi_s = M_C\\
&J_m\ddot{\varphi}_m + c_{rt}\left(\dot{\varphi}_m - \dot{\varphi}_r\right) + k_{rt}\left(\varphi_m - \varphi_r\right) = M_{fr2} + M_m
\end{aligned}
\tag{1}
$$

The Equation (1) is taken from literature [12] and presents a further development of the models found in [2], [7] and [13], where m_r, m_s, c, c_s, k, k_s are mass parameters, lateral damping coefficients and stiffnesses of the rotor and stator respectively, c_{rt}, c_{st}, k_{rt} and k_{st} are torsional damping coefficients and stifnesses of the rotor shaft and stator, e is the rotor mass eccentricity, J_r, J_s and J_m represent mass moments of inertia of the rotor, stator and induction motor respectively. M_{fr1} and M_{fr2} represent the torques of total losses (friction in bearings and losses in motor fan). These torques were identified from the measurements conducted on the test rig. To simplify the already complicated model, rotor and stator are assumed as isotropic regarding lateral stiffness and damping coefficient, what is still common practice in literature [14].

Vector $\mathbf{r_{r0}}$ from the Fig. 2 represents the static equilibrium position of the bowed shaft [13], where x_{r0} and y_{r0} are its X,Y components and are given by

$$
\begin{aligned}
x_{r0} &= r_{0x}\cos\varphi_r - r_{0y}\sin\varphi_r\\
y_{r0} &= r_{0x}\sin\varphi_r + r_{0x}\cos\varphi_r
\end{aligned}
\tag{2}
$$

Components r_{0x} and r_{0y} represent the static equilibrium position of the bowed shaft in the rotor fixed x,y,z coordinate system.

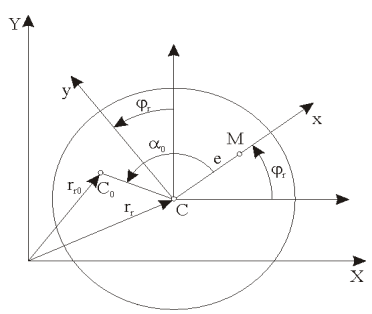

Fig.2. *Jeffcott rotor with a bowed shaft*

Contact forces F_{Cx} and F_{Cy} as well as the contact moment M_C are defined, according to Fig. 3, by the following expression:

$$\begin{aligned} F_{Cx} &= F_N \cos\gamma - F_T \sin\gamma \\ F_{Cy} &= F_N \sin\gamma + F_T \cos\gamma \\ M_C &= F_T\, R \end{aligned} \tag{3}$$

where the normal F_N and the tangential F_T contact forces have positive value when they are acting on the stator. Fig. 3 presents the geometry of the rotor - stator contact model with force definition.

1.2. Contact Models

Traditionally, for the rotor-stator impact modeling, two different methods have been applied, namely the Newton's restitution coefficient model and the Contact force-indentation model. The first model is based on the simplifying assumption of perfectly rigid bodies. Actual physical objects are compliant and hence the impact duration is strictly greater than zero. This more realistic view of impact phenomena led many researchers to consider the continuous-dynamics models of collision where bodies deform during impact and the collision dynamics is treated as a continuous-time dynamic phenomenon. In its general form, the force-indentation relationship looks like [15]:

$$F_N = F_k(\delta) + F_c(\delta,\dot{\delta}) + F_p(\delta,\dot{\delta}) \tag{4}$$

where, F_k is the elastic (conservative) part of the normal contact force F_N, F_c the viscous damping part and F_p the dissipative part due to plastic deformation. In the paper, plastic dissipations have been neglected. Fig. 4 shows the normal contact force model presented as a spring-damper system.

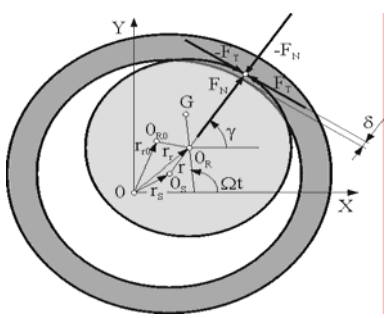

Fig.3. *Geometry of the rotor - stator contact model*

In the development of the elastic relation $F_k(\delta)$, the Hertz theory has to be mentioned. A very commonly used expression is the force-indentation relation for sphere to sphere contact, according to Hertz:

$$F_k = k_s \delta^{3/2} \tag{5}$$

where, F_k is the normal force pressing the solids together, δ represents the approach of two spheres, i.e. total deformation of both surfaces while k_s is a constant depending on the sphere radii and elastic properties of the sphere materials.

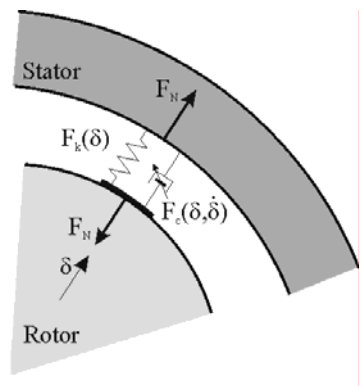

Fig.4. *Normal contact force model – a spring-damper system*

For the case of a cylindrical joint, Rivin [16] based his analysis on a half sine distribution of contact pressure between shaft and bearing. To calculate the pressure distribution, he considered two possible models for the force – deformation relation, linear and quadratic:

$$F_k = k_1 \delta \tag{6}$$

$$F_k = k_2 \delta^2 \tag{7}$$

Results of his experiments carried out with cast iron and hardened steel showed that the quadratic model offered a better correlation of the force deflection in a journal bearing when a high load per unit length was applied. For low loads, the linear model represented a better fit.

The simplest model of viscous dissipation $F_c(\delta,\dot{\delta})$ which is known from the literature [1] is a linear damper,

$$F_{\mathrm{c}} = c\dot{\delta} \tag{8}$$

where c is the viscous damping coefficient.

Non-linear expression for visco-elastic force, originally proposed by Hunt and Crossley [17], is given by

$$F_{\mathrm{c}} = \lambda \delta^{n} \dot{\delta} \tag{9}$$

where λ and n are model parameters. Fig. 5 shows responses of two analyzed models of the contact force regarding different combination of the elastic force models F_{k} and damping force models F_{c}.

The area bounded by hysteresis loop represents a loss of work during an impact of rotor and stator and can be expressed by,

$$W = \oint F_c \, \mathrm{d}x \tag{10}$$

The linear contact force model is described by the well known linear equation:

$$m\ddot{\delta} + c\dot{\delta} + k\delta = 0 \tag{11}$$

where c is the viscous damping coefficient, k is the stiffness, $\delta = |\mathbf{r}| - C_{\mathrm{r}}$ is the local deformation of the rotor and stator in the contact point in normal direction, $\dot{\delta}$ is the relative velocity of the rotor and stator along normal direction during the contact, $|\boldsymbol{r}| = \sqrt{(x_{\mathrm{r}} - x_{\mathrm{s}})^2 + (y_{\mathrm{r}} - y_{\mathrm{s}})^2}$ is the magnitude of vector difference between rotor and stator displacement according to Fig. 3 and C_{r} is the radial clearance between rotor and stator.

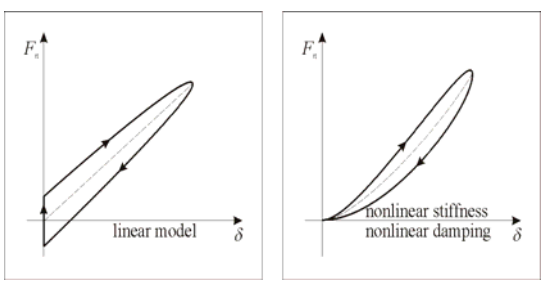

Fig.5. *Models of normal contact force*

In order to eliminate the negative forces that appear in the linear model and with the improvement in the sense of avoiding the discontinuity, Hunt and Crossley formulated the equation:

$$m\ddot{\delta} + \left(\lambda \delta^{\mathrm{n}}\right)\dot{\delta} + k\delta^{\mathrm{n}} = 0 \tag{12}$$

Their theory gives a relationship between restitution coefficient and dissipation in contacts via assumption of linear dependency of the restitution coefficient ε and initial impact velocity v_0 i.e.

$$\varepsilon = 1 - \alpha v_0 \tag{13}$$

Thus, according to [17] Equation (12) can be written in the following form

$$m\ddot{\delta} + k\delta^{n}\left(\frac{3}{2}\alpha\dot{\delta} + 1\right) = 0 \tag{14}$$

where α is the constant dependent mainly on material and geometry of bodies in contact. Based on Equation (14) two separate parts of normal contact force can be identified,

$$F_{\mathrm{N}} = F_{\mathrm{c}} + F_{\mathrm{k}} = \frac{3}{2}\alpha k\delta^{\mathrm{n}}\dot{\delta} + k\delta^{\mathrm{n}} \tag{15}$$

According to [16], index n can vary between 1 and 2 for cylindrical joints, so the choice of n = 3/2, originally proposed by Hertz (see Equation (5)), seems fairly reasonable.

In this paper both normal force models (linear–Equations (6), (8) and nonlinear–Equation (15)) have been used and compared.

Tangential contact force has been represented by the Coulomb dry friction law. The definition of the contact model described above can be expressed as follows

$$F_{\mathrm{N}} = \begin{cases} 0 & \text{for } r < C_{\mathrm{r}} \\ F_{\mathrm{k}} + F_{\mathrm{c}} & \text{for } r > C_{\mathrm{r}} \end{cases}$$
$$F_{\mathrm{T}} = \mu_{\mathrm{c}} F_{\mathrm{N}} \operatorname{sgn}(v_{\mathrm{sl}}) \tag{16}$$

where μ_{c} is the coefficient of friction and v_{sl} is the sliding velocity between rotor and stator surfaces in contact. The angle γ from equation (3) represents the normal force angle or direction of the smallest gap when rotor and stator are not in contact i.e.

$$\tan\gamma = \frac{y_{\mathrm{r}} - y_{\mathrm{s}}}{x_{\mathrm{r}} - x_{\mathrm{s}}} \tag{17}$$

To determine $\dot{\delta}$ and v_{sl} further vector calculation should be taken. Fig. 6 shows the velocity definition for the rotor and stator in contact. If the normal direction is known,

$$\boldsymbol{n}_0 = \frac{\boldsymbol{r}}{|\boldsymbol{r}|}, \quad \boldsymbol{r} = [r_x, r_y] = [x_r - x_s,\ y_r - y_s] \tag{18}$$

as well as the velocities of rotor and stator centers $\boldsymbol{v}_r = [v_{xr}, v_{yr}]$ and $\boldsymbol{v}_s = [v_{xs}, v_{ys}]$, one can easily obtain the relative normal rotor-to-stator velocity,

$$\dot{\delta} = v_{rn} - v_{sn} \tag{19}$$

where $v_{rn} = \boldsymbol{v}_r \cdot \boldsymbol{n}_0$ and $v_{sn} = \boldsymbol{v}_s \cdot \boldsymbol{n}_0$ represent the rotor and stator velocities in normal direction.

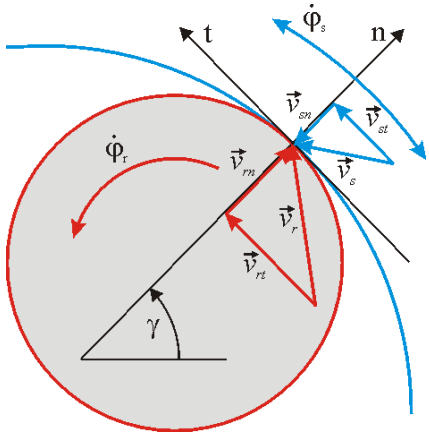

Fig.6. *Velocity definition for rotor and stator in contact*

The sliding velocity v_{sl} can be further defined as,

$$v_{sl} = v_{rt} - v_{st} \tag{20}$$

where $v_{rt} = \mathbf{v}_r \mathbf{t}_0 + \dot{\varphi}_r R$

and $v_{st} = \mathbf{v}_s \mathbf{t}_0 + \dot{\varphi}_s (R + C_r)$ represent the rotor and stator velocities on its periphery in tangential direction. R is the radius of the rotor while $\dot{\varphi}_r$, $\dot{\varphi}_s$ are angular velocities of the rotor and stator.

1.3. Mechanical Model of the Induction Motor

The driving moment of the induction electric motor has been modeled according to the Kloss expression [18] and [19]

$$M_m = M_{max} \frac{2 + 2s_{mn}}{\dfrac{s\varphi}{s_{mn}} + \dfrac{s_{mn}}{s\varphi} + 2s_{mn}} \tag{21}$$

where M_{max} and s_{mn} are the maximum motor torque or breakdown torque and slip for maximum motor torque, s is the actual slip of motors rotor with respect to the synchronous electromagnetic field and $\varphi = f_{sf}/f_s$ is the ratio of actual frequency given from frequency inverter and nominal frequency given by electrical network (f_s=50 Hz).

If we replace M_{max} in Equation (21) with $M_{max\,b} = -M_{max}(1+s_{mn})/(1-s_{mn})$, the Kloss expression for regenerative braking is obtained. The regenerative braking starts when actual speed of the motor's rotor is greater than the synchronous speed. The motor is then behaving as an electromagnetic brake. Fig. 7 shows the speed torque characteristics of an induction motor.

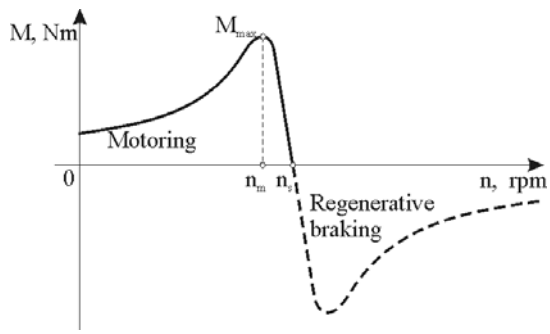

Fig.7. *Speed torque characteristics of an induction motor*

2 NUMERICAL SIMULATIONS

The numerical integration has been carried out by the fourth-order Runge-Kutta method. Time step of $\Delta t = 2 \cdot 10^{-5}$ s, has been applied in all simulations where the contact between rotor and stator was reasonably expected. Otherwise $\Delta t = 1 \cdot 10^{-4}$ s has been used. In some earlier simulations a greater time step was used but it turned out that it couldn't describe some specific rotor behaviors. Time step during one simulation has been fixed, so the subsequent frequency analysis could be done.

The parameters used in all calculations are as follows: rotor mass m_r = 4.25 kg, stator mass m_s = 3.838 kg, mass moments of inertia J_r = 4.532·10^{-3} kgm^2, J_m = 2.115·10^{-3} kgm^2, J_s = 2.11·10^{-2} kgm^2, rotor disc radius R = 0.06 m, stiffnesses k_r = 131540 N/m, k_{rt} = 1080 Nm/rad, k_s

= $1.237 \cdot 10^6$ N/m, k_{st} = 7917 Nm/rad, damping coefficients c_r = 22.43 Ns/m, c_{rt} = 0.0374 Nms/rad, c_s = 11.96 Ns/m, c_{st} = 0.0258 Nms/rad, radial clearance C_r = 0.4 mm, motor breakdown torque M_{max} = 10.25 Nm and motor speed of max. breakdown torque (at power network frequency f_s = 50 Hz) n_m = 2400 rpm.

The identified dependence between angular deceleration and angular velocity of the rotor, obtained from free run down tests (induction motor switched off), had the following form

$$\varepsilon = -4 \cdot 10^{-6} \omega^3 + 0.002\omega^2 - 0.5376\omega - 10.513 \quad \text{rad/s}^2 \tag{22}$$

2.1. Numerical Simulation of Motor Controlled Run-Down (RD) Analysis

The numerical RD analysis has been performed to identify the basic dynamic characteristics of the rotor-stator system and to correlate them with the experimental results. Knowing, from the modal testing (rotor response on the impulse force excitation at standstill) that the first rotor natural bending frequency is equal to f_{r1} = 28.0 Hz and according to the Jeffcott (or Laval) theory it is the only natural frequency, RD analysis has been focused on speed range n = 40 to 0 Hz. The second rotor natural bending frequency obtained by the modal testing has been f_{r2} = 148.5 Hz hence it has been far away enough from the first natural frequency and its influence has been negligible.

The basic goal of this part of numerical analysis was to discover the appropriate relation of the mass unbalance eccentricity vector **e** and the static equilibrium position of the bowed shaft $\mathbf{r_{r0}}$ according to the measured maximum lateral displacement amplitude of the rotor disc and the qualitative shape of the rotor lateral response in time domain, Fig. 8. Final parameters have been e = 0.046 mm, r_{r0} = 0.05 mm and phase lag of the **e** in relation to $\mathbf{r_{r0}}$ i.e. $\alpha_0 = \pi$ rad (see Fig. 2). RD analysis has been controlled by a linear frequency ramp (speed law) of the synchronous electromagnetic field of induction motor, f_{sf} = 40 to 0 Hz in the time period of 34 s, while its rotor behaved according to the presented mechanical model. At the beginning of the numerical simulation, 2 s have been taken additionally for disappearance of any transients caused by initial conditions.

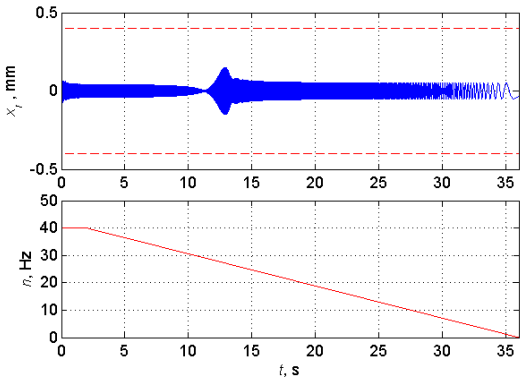

Fig.8. *Simulated lateral rotor response in horizont direction for RD analysis and speed law*

Fig. 9 shows the spectral map of the lateral rotor response in the horizontal direction where as expected only the first order can be seen. On the same figure at the beginning of the simulation, the rotor critical speed is excited but only because of the numerical transient due to initial conditions.

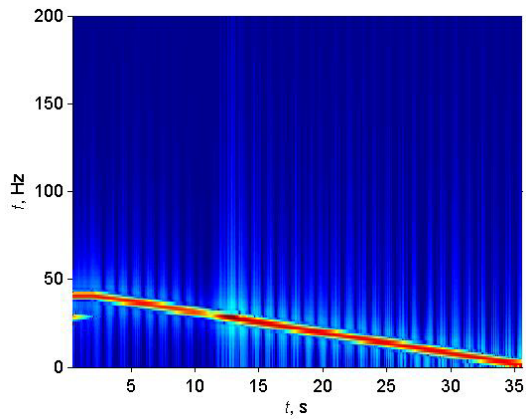

Fig.9. *Spectral map of the lateral rotor response in horizontal direction x_r*

2.2. Numerical Simulations of Sudden Rotor Unbalance Increase (SRUI) Analysis

The basic assumption has been that the rotor is running at a nominal speed above the first rotor critical speed and that the rotor is well balanced. To achieve the initial condition which is similar to the steadily running speed and to avoid any transients, the sudden unbalance was introduced 1 second after the start of simulation. After sudden appearance of the additional unbalance m_{add} it has been assumed that the

permanent monitoring system of the turbo machine has recorded unallowable vibrations and as a precaution measure it starts an immediate shut down procedure. This was accomplished by switching off the induction motor. Then the whole rotor starts to decelerate due to given torques of losses, expressed by the identified rotor angular deceleration mentioned above. The rotor is then approaching to its critical speed and because of additional unbalance m_{uadd} it contacts the stator. When the additional unbalance is big enough, the rotor contacts the stator immediately after appearance of the additional unbalance i.e. before switching off the motor. The time period for response of the shut down procedure after sudden unbalance appearance has been set to 1 s. Two different contact normal force models have been compared i.e. linear and nonlinear. Linear model has contact stiffness $k_{\mathrm{C}} = 7.7 \cdot 10^7$ N/m and contact damping $c_{\mathrm{C}} = 3.2 \cdot 10^3$ Ns/m and nonlinear model has contact toughness $k_{\mathrm{C}} = 1.8 \cdot 10^8$ Pa/m$^{1/2}$ and parameter $\alpha = 3$ s/m. The output inverter frequency before unbalance appearance was set to $n_{\mathrm{sf}} = 40$ Hz. It turns out that the frictional losses in test rig are quite big so the rotor decelerates, with small unbalance and without contact, in some 5 to 6 seconds from 40 Hz to standstill.

In Figs. 10 to 12 the rotor response without contact to stator is presented, without any additional unbalance, $m_{\mathrm{add}} = 0$ (or presented via rotor mass eccentricity $e_{\mathrm{add}} = 0$). If someone compares Fig. 9 and Fig. 12, except differences in the shape of first order (linear in Fig. 9 and nonlinear in Fig. 12), on Fig. 12 exists additional horizontal line at 28 Hz. The reason for this mainly lies in fast rotor speed change while passing though its critical speed.

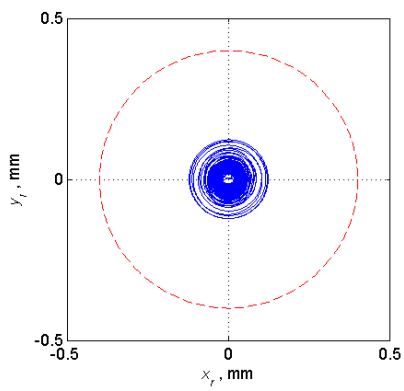

Fig.10. *Rotor center orbit during free RD (red dashed line represents a clearance circle)*

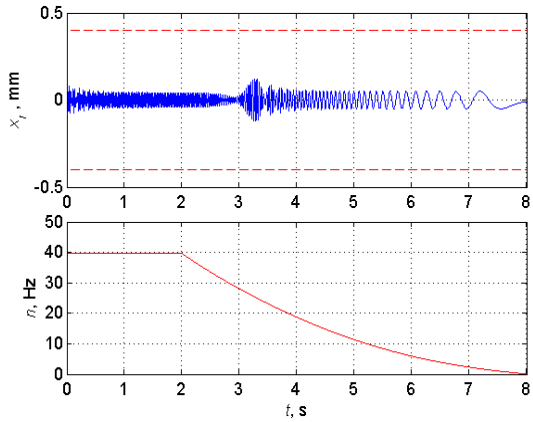

Fig.11. *Simulated lateral rotor response in horizontal direction for free RD analysis with speed law $e_{add} = 0$*

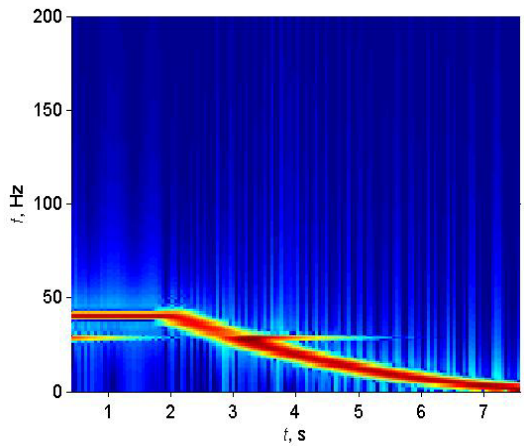

Fig.12. *Spectral map of rotor displacements in horizontal direction, free RD, $e_{add} = 0$*

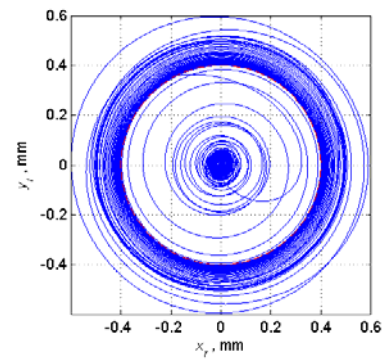

Fig.13. *Rotor center orbit during RD, rotor-stator contact appeared, $e_{add} = 0.124$ mm*

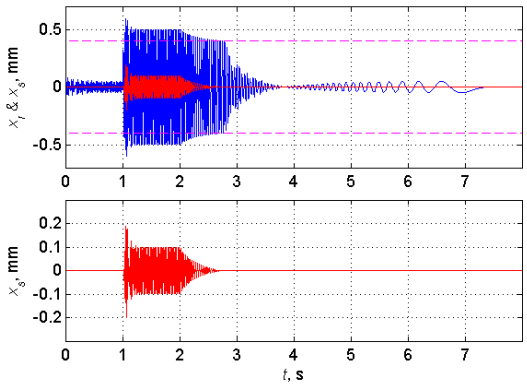

Fig.14. *Lateral rotor and stator responses in horizontal direction, contact appeared, e_{add} = $1.24 \cdot 10^{-4}$ m, r_{r0} = 0.05 mm, $\alpha_0 = \pi$ rad*

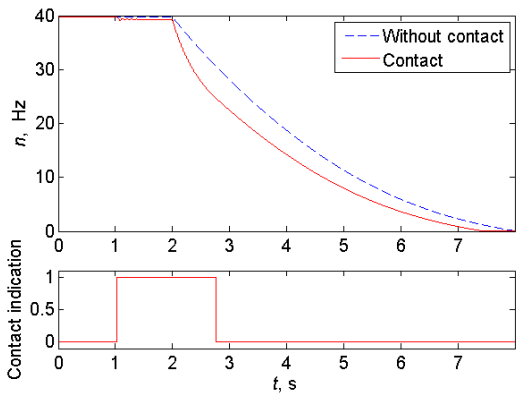

Fig.15. *Rotor speed laws for simulations without and with contact*

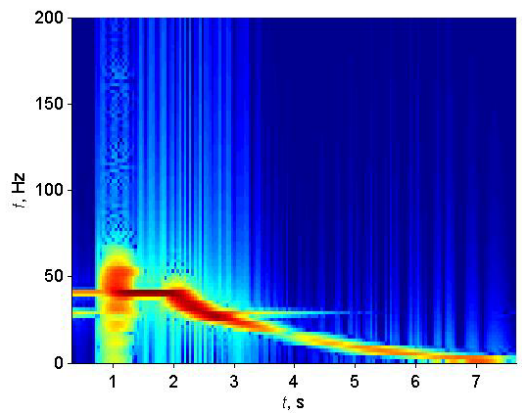

Fig.16. *Spectral map of rotor displacement in horizontal direction, contact appeared*

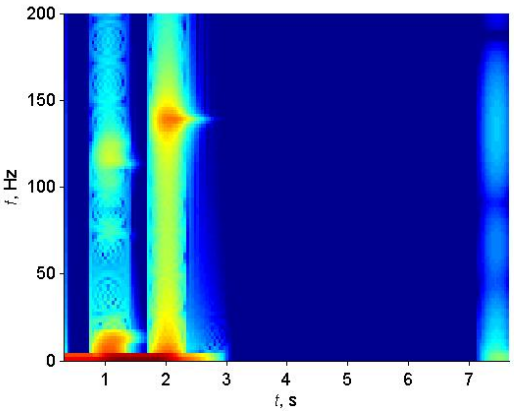

Fig.17. *Spectral map of rotor relative torsional angles φ_m - φ_r, contact appeared*

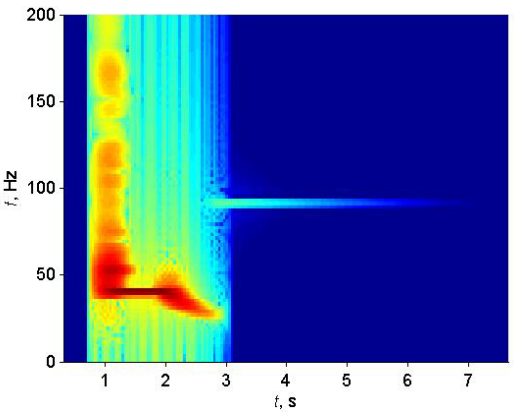

Fig.18. *Spectral map of stator lateral velocities in horizontal direction, contact appeared*

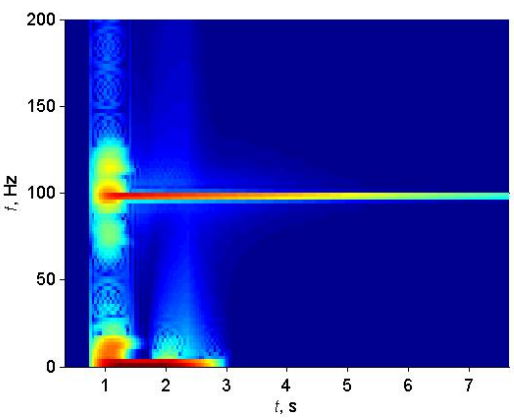

Fig.19. *Spectral map of stator torsional angles, contact appeared*

Figures 13 to 19 show rotor and stator response after the appearance of the additional mass unbalance (presented in rotor mass eccentricity) e_{add} = 0.124 mm, so the total rotor mass eccentricity is equal to $e = e_{in} + e_{add}$ =1.17 mm. The magnitude of the vector $\mathbf{r_{r0}}$ was r_{r0} = 0.05 mm and the phase lag was $\alpha_0 = \pi$ rad. In this simulation the linear model of normal contact force has been applied and coefficient of friction in contact was μ_C = 0.18, according to Bartha [2].

In Fig. 11 we had the supercritical self-balancing effect because the mass eccentricity e was smaller than the magnitude of the shaft bow vector r_{r0}. On the contrary in Fig. 14 the self balancing effect is placed subcritically at the t_1 = 3.8 s of simulation because after sudden unbalance increase, the total mass unbalance eccentricity e became greater than r_{r0}.

Fig. 15 shows the difference between speed laws for simulations with and without the rotor-stator contact appearance. As expected a rotor deceleration for simulation where the rotor-stator contact appeared, was more intensive especially in a time period with established rotor-stator contact (see contact indication in Fig. 15). After introduction of SRUI, the rotor made several impacts to the stator and then a permanent contact was established. In Figs. 16 to 19 there is a narrow time period around t_1 = 1 s of simulation where multiple harmonics can be seen. This is due to intermittent rotor-stator contact. It is interesting to see after the rotor-stator separation (t_1 = 2.75 s) that the rotor and stator continued to vibrate with their own flexural natural frequencies, f_r = 28 Hz (Fig. 16), f_s = 90 Hz (Fig. 18) and torsional frequencies f_{rt} = 137.9 Hz (Fig. 17), f_{st} = 97.7 Hz (Fig. 19).

In Fig. 20, the influence of the phase lag of the mass unbalance eccentricity vector **e** in relation to the static equilibrium position of the bowed shaft $\mathbf{r_{r0}}$ i.e. α_0 has been analyzed. Presented contact forces are related to α_0 = 180º, 135º and 90º. In the same time normal contact forces of the linear and nonlinear models have been compared, so the diagrams in the left column correspond to the linear and in the right column to the nonlinear model of the normal contact force.

The main difference between the linear and nonlinear model of the contact normal force, presented in Fig. 20, can be seen in the region immediately after appearance of SRUI. Nonlinear model generally had a greater force response for the first impact, while in permanent contact both linear and nonlinear model had almost the same values. Details about the differences between analyzed normal force models and influence of the phase lag α_0 are presented in Table 1.

The normal force for the permanent rotor-stator contact (with sliding) F_{Cperm} has showed expected increasing trend with decreasing phase lag α_0, because α_0 smaller than 180° means greater unbalance excitation. The reason for contradictory trend of decreasing of the F_{Cmax} (max. value of the normal force for the first impact) with decreasing α_0 (increasing unbalance excitation) lies in the fact that α_0 of the e_{in} and e_{add} is the same. This caused an increasing tendency of the radius of initial rotor orbit and therefore the decrease of the maximum normal velocity at the first rotor-stator impact.

Table 1. *Results of contact normal force analysis regarding phase lag of the mass eccentricity vector e in relation to shaft bow radius vector r_{r0}*

α_0,	F_{Cmax} / F_{Cperm} , N	
	Linear	Nonlinear
180°	327.7 / 96.8	611.9 / 97.1
135°	279.8 / 99.3	462.2 / 99.5
90°	203.7 / 104.8	277.1 / 105.0

3 EXPERIMENTAL ANALYSIS

The analysis has been performed on the test rig which can be seen on Fig. 21. The test rig has been specifically designed for the rotor-stator contact measurements. It consists of the following main components: robust foundation, mounting plate, roller bearings with their supports, rotor, stator, flexible coupling, induction motor with speed controller, measuring system based on Bruel and Kjaer non-contacting displacement sensors and National Instruments data acquisition card PCI NI 4472 with adequate software (LabVIEW, Matlab). Measurements showed that the first critical speed of the rotor was 28 Hz, while the first natural frequency of the stator was 90 Hz. Radial clearance between the rotor and stator was 0.4 mm. Before the experiments the rotor had been balanced.

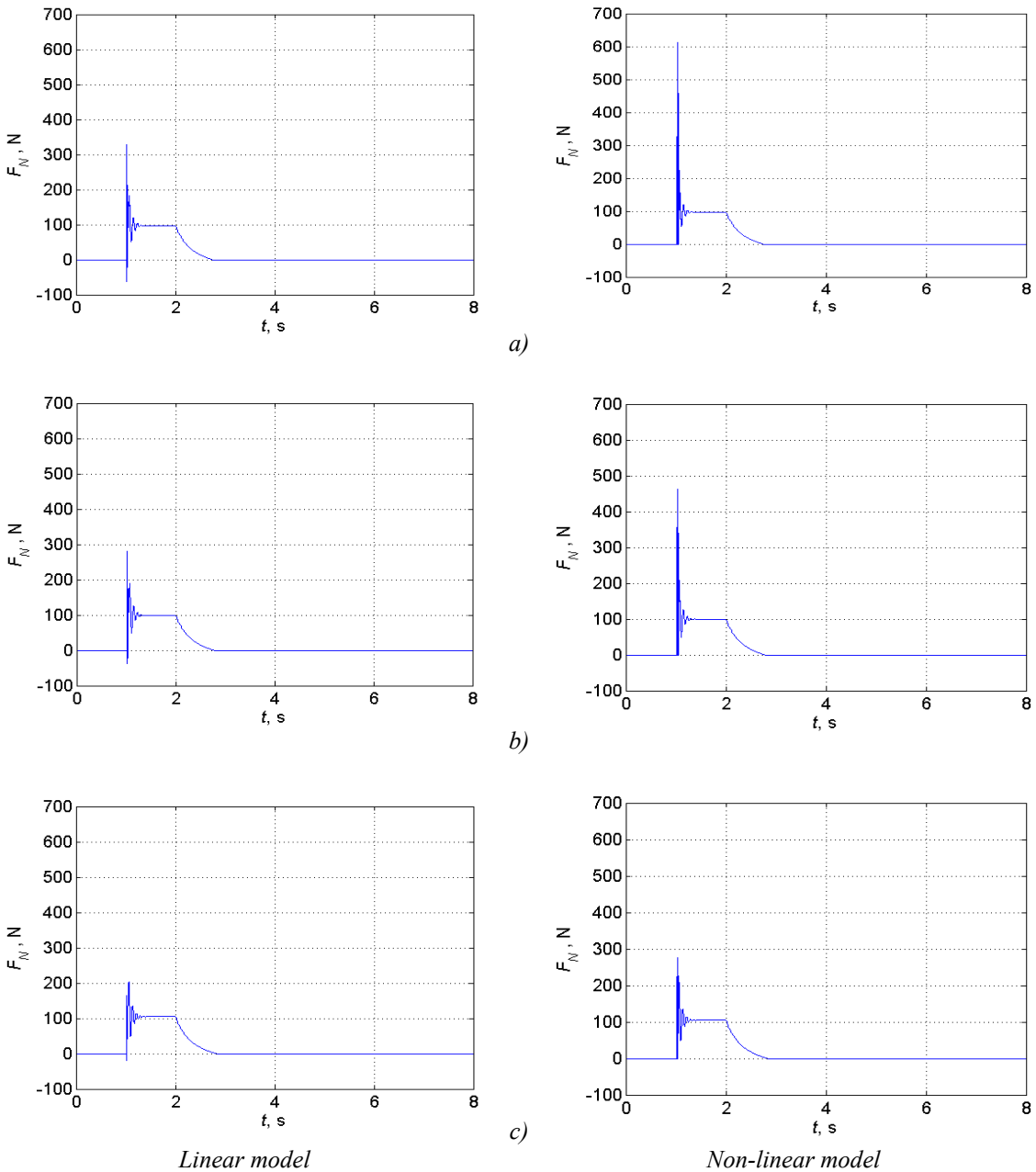

Fig. 20. *Normal forces in contact between rotor and stator; left column – linear model, right column nonlinear model; a) $\alpha_0 = 180°$, b) $\alpha_0 = 135°$, c) $\alpha_0 = 90°$*

Also before every single experiment the contact surfaces of the rotor and stator were lubricated with WD40 spray [2] to decrease the coefficient of friction to the value of approximately $\mu = 0.18$ and to minimize the possibility of destruction of sensors and other structural parts of the test rig.

3.1 Experimental, Motor Controlled, Run-Down (RD) Analysis

To verify the numerical results presented in chapter 2.1, an experimental RD analysis has been performed.

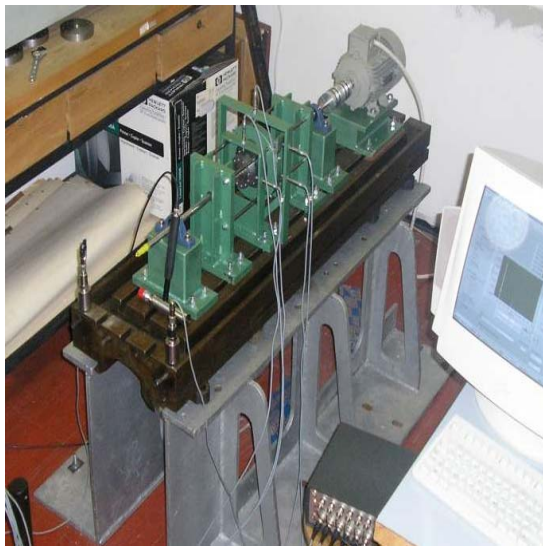

Fig.21. *Test rig for rotor-stator contact investigation*

The speed change has been controlled via frequency inverter Micromaster 440 from Siemens. The speed rate has been the same as in the numerical simulation only the starting speed has been 70 Hz. Figs. 22 and 23 show measured lateral responses of the rotor in horizontal x direction with speed law and spectral map of the rotor lateral response in the horizontal direction. This figures can be compared to Figs. 8 and 9 respectively, for a speed range n = 40 to 0 Hz. In Fig. 23 except for the first harmonic, other higher harmonics can be also seen due to various imperfections of the experimental model like radial and angular misalignment etc. Fig. 24 shows a spectral map of stator displacements in horizontal direction. Although there wasn't direct contact between the rotor and stator, the stator was excited as it can be seen on Fig. 24. This is due to the fact that rotor bearing supports and stator supports are rigidly connected on the mounting plate, so this situation allows an indirect stator excitation through the mounting plate.

Measured flexural natural frequencies were, f_r = 28 Hz (Fig. 23), f_s = 90 Hz (Fig. 24) and stator torsional frequency f_{st} = 102.5 Hz (Fig. 24).

To excite effectively both stator natural frequencies (with second harmonic), the 70 Hz as a starting speed of this RD analysis was chosen.

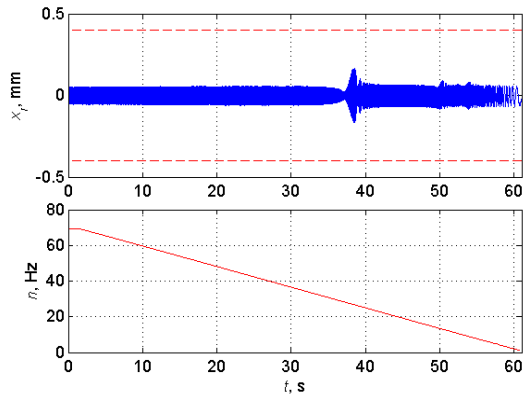

Fig.22. *Measured lateral rotor x_r response in horizontal direction and speed law*

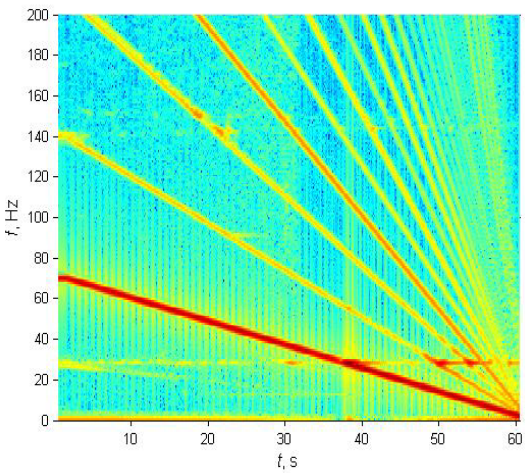

Fig.23. *Measured spectral map of rotor displacement in horizontal direction*

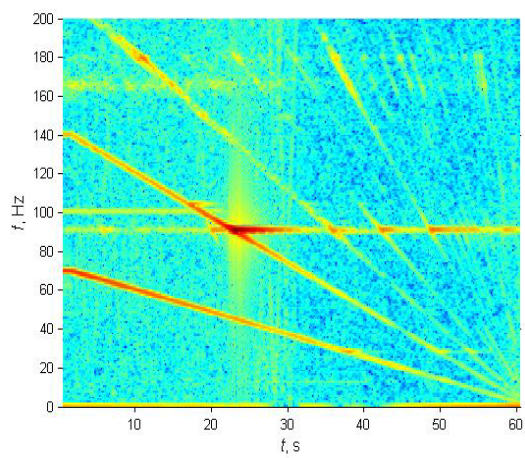

Fig.24. *Measured spectral map of stator displacement in horizontal direction*

3.2 Experimental Sudden Rotor Unbalance Increase (SRUI) Analysis

Because this test rig couldn't simulate the SRUI scenario during the rotor operation, additional mass has been added instead of being removed but with rotor at standstill. The rotor has been quickly accelerated to rotational speed of 40 Hz to reduce the rubbing while passing through rotor critical speed. The power supply to the motor was then switched off and a whole rotor started a free deceleration. Two measurements have been presented: free rotor RD with good rotor balance condition as in previous analysis (without appearance of the rotor-stator contact), Figs. 25 and 26 and free RD of the rotor with additional mass unbalance (presented in the rotor mass eccentricity) e_{add} = 0.124 mm, Figs. 27 to 30.

The first measurement (Figs. 25 and 26) can be compared directly with the numerical simulation presented in the Figs. 11 and 12. Looking just on Figs. 11 and 25 a great correspondence can be noticed. Comparing spectral maps of simulated and measured lateral rotor displacements, i.e. Figs. 12 and 26, some differences regarding presence of higher harmonics in measured response can be observed. The reason for their presence is explained in the previous chapter and their influence is reflected on extended life of rotor bending natural frequency present in the response till the rotor standstill.

The second measurement (Figs. 27 to 30) can be compared with the numerical simulation presented in Figs. 13 to 19 with remark that in simulation the motor is switched off in t_1 = 2 s (Fig. 14) while in measurement in t_1 = 1.65 s. Furthermore, rotor and stator were, in measurement, in permanent contact from the very beginning, while in numerical SRUI simulation they got into contact after additional mass unbalance activation i.e. in t_1 = 1.0 s of simulation.

Taking into account the aforementioned reasons for differences between simulation and measurement, a great correspondence between Figs. 14 and 27 can be noticed again. In measured spectral map of the rotor lateral response, Fig. 28, vibrations have strong first harmonic component i.e. 1× rotating frequency, while there are higher harmonics too. They were present also in the rotor lateral response without appearance of the rotor-stator contact (Fig. 26), because of the above mentioned imperfections of the rotor experimental model. Both lateral and torsional natural frequencies of the stator are present in each of its depicted responses, i.e. in the lateral response (Fig. 29) and in the torsional response (Fig. 30), after the final rotor-stator separation. This happened mainly because of the vicinity of stator natural frequencies and due to indirect measurement of torsional stator rotations via 2 parallel non-contacting displacement sensors in horizontal (lateral) direction. Although both stator frequencies can be seen in two separated responses, lateral frequency is more emphasized in lateral response while torsional frequency is more emphasized in its torsional response. Thus in the case of torsionally elastic systems susceptible to the rotor-stator contact it is important to combine the measurements with results of the numerical simulations to make a decision of the character of a particular natural frequency.

4 CONCLUSIONS

The presented numerical model of the rotor with a bowed shaft – stator system has proved to be capable for analyzing different contact situations. Linear and nonlinear normal contact force models were compared in the same simulated situations and they showed similar responses for permanent rotor-stator contact, while nonlinear force model generally had a greater response for the first rotor-stator impact. This didn't have a big influence on a subsequent rotor and stator response and their stability, for the analyzed parameters. Both normal force models, for permanent rotor-stator contact (with sliding) F_{Cperm}, showed increasing tendency with decreasing phase lag α_0, because if α_0 is smaller than 180° the unbalance excitation will be greater.

Experimental analysis showed more realistic rotor and stator responses with more different harmonics present than in the results of numerical simulations. This was mainly due to tested model imperfections and measuring principle. In the real practice measured signals are even more unclear and mixed with different noise, so it is important to combine the measurements with adequate numerical simulations to recognize the needed information.

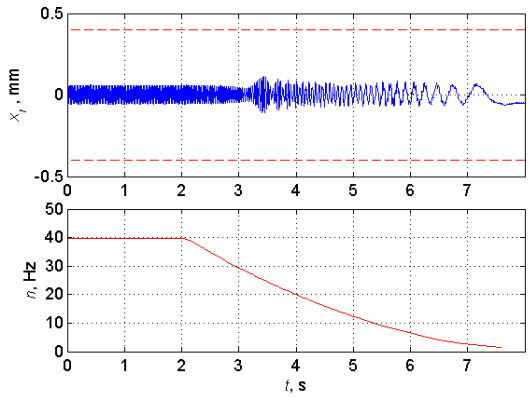

Fig.25. *Measured lateral rotor x_r response in horizontal direction with speed law, contact-free situation, free RD, e_{add} = 0 mm*

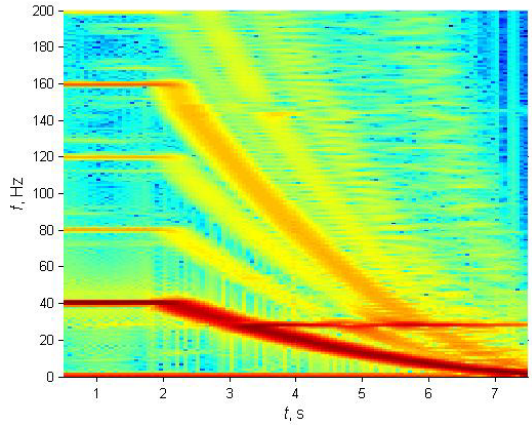

Fig.26. *Spectral map of rotor displacements in horizontal direction, free RD, e_{add} = 0 mm*

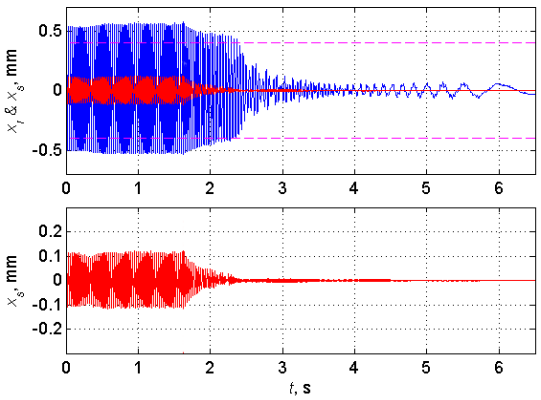

Fig.27. *Measured lateral rotor x_r and stator x_s responses in horizontal direction, free RD, contact appeared, e_{add} = 0.124 mm*

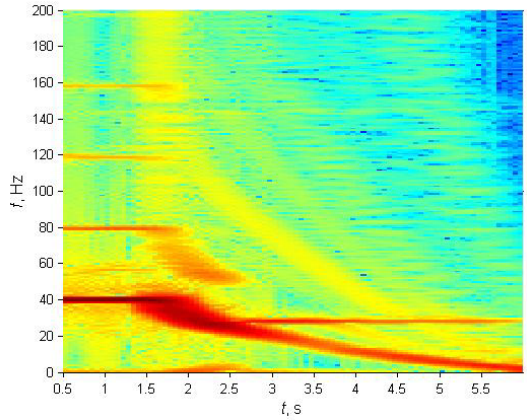

Fig.28. *Spectral map of rotor lateral displacements in horizontal direction, free RD, contact appeared, e_{add} = 0.124 mm*

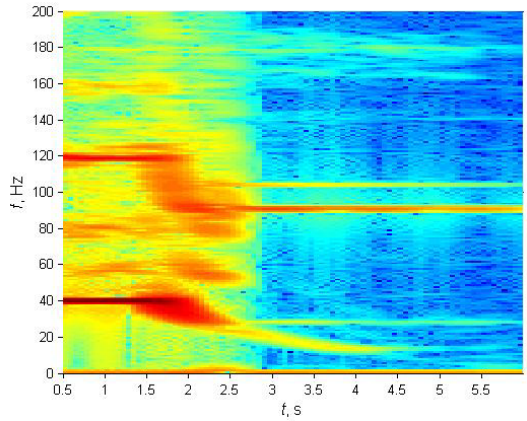

Fig.29. *Measured spectral map of stator lateral displacement in horizontal direction, free RD, e_{add} = 0.124 mm*

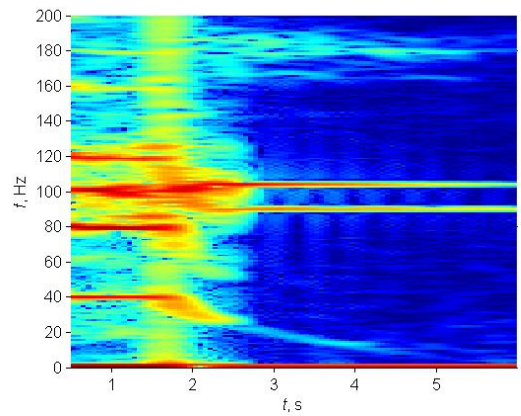

Fig.30. *Measured spectral map of stator torsional rotations, free RD, e_{add} = 0.124 mm*

5 REFERENCES

[1] Choy, F. K., Padovan, J. (1987) Non-linear transient analysis of rotor-casing rub events, *Journal of Sound and Vibration*, 113(3), pp. 529-545.

[2] Bartha, A. R. (2000) Dry Friction Backward Whirl of Rotors, PhD. Thesis, *Swiss Federal Institute of Technology Zurich*.

[3] Von Groll, G., Ewins, D. J. (2002) A Mechanism of Low Subharmonic Responce in Rotor/Stator Contact – Measurement and Simulation, *Journal of Vibration and Acoustics*, vol. 124 (2002), pp.350.-358.

[4] Ahrens, J., Jiang, J., Ulbrich, H., Ahaus, G. (2001) Experimentelle Untersuchungen zum Schaufelanstreifen, *Schwingungen in rotierenden maschinen – SIRM V Tagung*, Wien, Austria, pp. 97-108, (in German).

[5] Fumagalli, M., Schweitzer, G. (1994) Impact dynamics of high speed rotors in retainer bearings and measurement concepts, *4th International Symposium on Magnetic Bearings*, ETH Zurich Switzerland.

[6] Orth, M., Nordmann, R. ANEAS (2002) A modeling tool for nonlinear analysis of active magnetic bearing systems, *2nd IFAC Conference on Mechatronic Systems*, Berkley, USA, pp. 357-362.

[7] Edwards, S., Lees, A. W. and Friswell, M. I. (1999) The Influence of Torsion on Rotor/Stator Contact in Rotating Machinery, *Journal of Sound and Vibration*, 225(4), pp. 767-778.

[8] Žigulić, R., Butković, M., Braut S. (2002) Nonlinear dynamics of multi-disc rotor in dry friction bearings, *IFToMM Sixth International Conference on Rotor Dynamics*, vol. 2, Sydney, Australia, pp. 960-967.

[9] Karpenko, E.V., Pavlovskaia, E.E., Wiercigroch, M. (2003) Bifurcation analysis of a preloaded Jeffcott rotor, *Chaos, Solitons & Fractals*, 15, pp. 407–416.

[10] Pavlovskaia, E.E., Karpenko, E.V., Wiercigroch, M. (2004) Nonlinear dynamics of a Jeffcott rotor with a preloaded snubber ring, *Journal of Sound and Vibration*, 276 (1–2), pp. 361–379.

[11] Karpenko, E.V., Wiercigroch, M., Pavlovskaia, E.E., Neilson, R.D. (2006) Experimental verification of Jeffcott rotor model with preloaded snubber ring, *Journal of Sound and Vibration*, 298, pp. 907-917

[12] Braut, S (2006) Analysis of the rotor-stator contact dynamics, PhD thesis (in Croatian), University of Rijeka, Faculty of Engineering, Rijeka.

[13] Childs, D. W. (1993) Turbomachinery Rotordynamics, Phenomena, Modeling, and Analysis, *John Wiley & Sons*, New York.

[14] Chu, F., Lu, W. (2007) Stiffening effect of the rotor during the rotor-to-stator rub in a rotating machine, *Journal of Sound and Vibration*, 308(2007), 758-766.

[15] Faik, S., Witteman, H. (2000) Modeling of Impact Dynamics: A Literature Survey, *2000 International ADAMS User Conference*, Orlando, Florida, USA, pp. 1-11.

[16] Rivin, E. I. (1999) Stiffness and Damping in Mechanical Design, *Marcel Dekker, Inc*. New York.

[17] Hunt, K. H. and Crossley, F. R. E. (1975) Coefcient of restitution interpreted as damping in vibroimpact, *Transactions of the ASME, Journal of Applied Mechanics*, pp. 440-445.

[18] Jurković, B. (1990) Electric power drivers, *Školska knjiga*, Zagreb, (in Croatian).

[19] Boldea, I., Nasar, S. A. (2002) The Induction Machine Handbook, *CRC Press*, Boca Raton.